

Composition determination of multinary III/V semiconductors via STEM HAADF multislice simulations.

Lennart Duschek¹, Andreas Beyer¹, Jan Oliver Oelerich¹ and Kerstin Volz¹

¹Materials Science Center and Faculty of Physics, Philipps-Universität Marburg
Hans-Meerweinstraße 6, 35032 Marburg, Germany,
lennart.duschek@physik.uni-marburg.de, Tel +49 6421 28 25610

Abstract

Knowledge of the microscopic elemental composition of multinary III/V semiconductor materials is crucial to the development of functionalized opto-electronic devices. Well-proven composition analysis methods, such as high resolution X-ray diffraction (XRD), fail to determine the elemental composition when more than three atomic species are involved. In this work we propose a procedure for the composition analysis of multinary III/V semiconductors at atomic resolution using high angle annular dark field (HAADF) scanning transmission electron microscopy (STEM) image simulations. Our method exploits the dependence of HAADF-STEM image intensities on the atomic number and static atomic displacements (SADs) at different detector inner angles. Here, we describe the proposed method in detail using Ga(NAsP) as an example multinary material.

Motivation

A key issue in the development process of any novel functional material, e.g. a new compound semiconductor material or a device, is to gather information about the exact composition as well as elemental distribution on atomic length scales. For ternary materials, the method of choice to obtain laterally averaged information is high resolution X-ray diffraction (HRXRD) [1], where the elemental composition is determined via the lattice constant of the material by assuming Vegard's law [2,3]. For quaternary layers where the former is not possible, Tilli et al. proposed a method that uses the (002) reflection's peak intensity of a single XRD measurement combined with the strain of the layer, to determine the composition of Ga(NAsP) layers with layer thicknesses up to 30 nm [4]. The quantitative analysis of scanning transmission electron microscopy (STEM) images has made a big progress over the last two decades [5–8]. A comparison of the mean intensity from STEM high angle annular dark field (HAADF) images with STEM multislice simulations [9] can also reveal the elemental composition of the TEM specimen [10–12], as well as give information about chemical homogeneity in ternary alloys [10,13,14] at nanometer length scales. The latter technique uses the fact that the intensity of a STEM image is proportional to the mean atomic number Z of the atom species [15–17]. With an aberration corrected microscope, this technique is also suitable for quantifying material composition at atomic length scales [10,18]. Müller-Caspary et al. recently showed the use of angular resolved high resolution STEM to determine the N composition in a Ga(NAs) [19] multi-quantum well structure. The rather straight-forward interpretation of the so-called Z-contrast images becomes complicated for quaternary or even more-component semiconductor alloys, which are essential to achieve the desired band-gap/lattice constant combination for many semiconductor devices, e.g. (GaIn)(NAs) or (GaIn)(NAsSb) for solar cells [20]. The images obtained from STEM measurements are always a projection of the crystal's atomic potentials in the electron (e^-) beam direction. For atomic columns containing more than two different elements, the ADF intensity is ambiguous as an increasing amount of a low- Z element can always be compensated by a decrease of a heavier atomic species, preserving the mean atomic number. A method where the additional

information required to quantify the composition in not atomically resolved STEM HAADF images comes from the measurement of the strain state of the quantum well, is presented by Grieb et al. in Ref. [21] with the example of (GaIn)(NAs). For this material system, it would in principle also be possible to derive the atomic composition on each sublattice, group III as well as group V, from high resolution STEM images, since each sublattice of this quaternary alloy consists only of a mixture of two atomic species. However, the method cannot be applied if one sublattice is composed of more than two atom species.

In this work, we propose a new procedure for the compositional analysis of multinary semiconductor alloys. This procedure aims to find the best fit between experimental and simulated high resolution STEM images, and allows for more than two elements on one atomic column. Here we will focus on the procedure itself without providing application examples, which will be subject of upcoming publications. The method exploits the different behavior of the scattered intensity at the positions on and off the atomic columns (in the background), respectively, and at different detector inner angles in simulated ADF images. We apply the procedure to the model system $\text{Ga}(\text{N}_x\text{As}_{100-x-y}\text{P}_y)$, a III/V semiconductor with a cubic zinc-blende crystal structure, the composition mixture solely occurs on the group V sublattice. It is important to note that the N incorporated in the material evokes crystal distortions called static atomic displacements (SAD) that have influence on the ADF intensity [22]. The SAD are the key to our method as we will show in the next section. The Ga(NAsP) material system was chosen as an example, as it has a tremendous application potential in the integration of optically active photonic devices on Silicon substrates [23–25]. However, the method presented here can be applied to any multinary crystalline material, where composition affects the scattered intensity at distinct spatial positions and/or at different detector angles.

Method

In the method presented here, we compare HAADF STEM intensities from a set of multislice STEM simulations, split into group III, V and background (BG) positions, i.e. the positions between the atomic

columns. The set contains numerous simulations with systematically varied N and P composition for the chosen example of Ga(NAsP).

The super cells used for the multislice simulations were 5 x 5 unit cells (approx. 2.5 nm x 2.5 nm) wide and have a thickness of up to 60 unit cells (approx. 30 nm) in the electron beam direction, fitting in the typical thickness range of conventionally prepared TEM specimens of around 15 nm – 30 nm. Both the N and the P atoms were distributed randomly on the group V lattice positions of a GaAs matrix and the resulting cell was relaxed via a valence force field (VFF) routine [26]. Structural relaxation is important when trying to match simulations as closely as possible to the real specimen. The SAD have a huge influence on the local intensity distribution [27] and thus are a key element for this technique. To underpin this statement the complete procedure will also be carried out with a simulation set built from unrelaxed super cells. The numerical simulations were performed with the STEMsalabim software package [28] based on the multislice algorithm of Kirkland [29,30]. This software package is designed for highly parallelized simulations on high-performance computer clusters. A more detailed description on the technical implementation and scaling of this code can be found in Ref. [28]. Thermal diffuse scattering (TDS) was taken into account using the frozen lattice approach [31], where the atomic positions get displaced statistically (Gaussian distribution) from their resting positions. Geometric aberrations were chosen to fit the parameters of a spherical aberration corrected microscope, namely the JEOL JEM-2200 FS, with $C_s = 2$ μm , $C_5 = 5$ mm, $\Delta f = -2$ nm, and a convergence semi-angle of 24 mrad. Chromatic aberration was taken into account with a defocus series as proposed in Ref. [32–35]. A two dimensional Lorentzian function with a full width at half maximum of 36 pm was convoluted with the image to model the source size of the electron gun [32]. Furthermore the detector sensitivity was determined and applied to the simulation as proposed by LeBeau et al. in Ref. [7]. This was done to match the simulations as closely as possible to experimental STEM images.

The sampling of the simulation set was chosen to be in the range of experimentally reasonable compositions of N (0 – 20 %) and P (0 - 30 %) with a step size of 2 %, resulting in 150 single concentration steps. For each concentration point, a defocus series with 7 defoci and 10 phonon configurations (TDS), was calculated. A new set of phonon configurations was used for each defocus, resulting in 70 independent phonon configurations for each concentration point. With this, a total of 10500 simulations was performed. Each result was stored as a compressed binary file using NetCDF [36]. To save disk space, the phonon configurations for each defocus were averaged leading to a file size of approx. 500 MB per simulation. The total amount of file space covered by the complete simulation set sums up to roughly 750 GB. The simulation time for one concentration point parallelized over 128 computing nodes was about 11 hours. Assuming that the simulation time scales almost linearly, the simulation time on a single desktop PC with 8 computing cores would take 26400 hours or approximately 3 years. With the computational resources of a mid-sized cluster, on the other hand, the total simulation time for the whole concentration map is about 2 weeks, since many simulations can run simultaneously. Besides the long simulation time, the file size of one concentration point is about 4 GB which means that only one file at a time fits into the memory of a common desktop computer with 8 GB of RAM. By using the principle of selective data loading and parallelizing this step to the 8 threads of a modern desktop machine, a processing time of approx. 5 min was achieved to gather information from the whole simulation set.

Results

In the following paragraph, we will first explain the transformation of the multislice simulation set into *composition maps* that represent the integrated STEM intensity on distinct spatial positions. Afterwards we will discuss the simulated *composition maps*, built from the unrelaxed as well as the relaxed super cell set, for a high angular range of $\theta_{in-out} = 71 - 174$ mrad which will be referred to be the HAADF regime from now on. We will then investigate the *composition maps* for a low angular range, namely

$\theta_{in-out} = 34 - 136$ mrad and will refer to this as low angle ADF (LAADF) regime. In the LAADF regime we will also look at the *composition maps* built from the unrelaxed and the relaxed super cell set with a focus on the angular dependence of the SAD effect. In the end, *composition maps* will be combined and a sanity check of the presented algorithm with three exemplarily chosen $\text{Ga}(\text{N}_x\text{As}_{100-x-y}\text{P}_y)$ compositions is performed.

The basis of the presented method is a set of simulations with systematically varied N - P concentration as explained in the previous section. Every red mark in Figure 1 represents a full STEM multislice simulation. With given simulation parameters, including the detector range θ_{in-out} and sensitivity θ_{sen} , chromatic as well as geometric aberrations, and sample thickness t , a HAADF image is formed. The atomic column positions are found by a 2D peak finding algorithm, implemented in a custom MATLAB script and divided into group III and V atomic column positions. Afterwards, the BG positions are determined by finding the center of mass between 4 neighboring atomic columns (Figure 1).

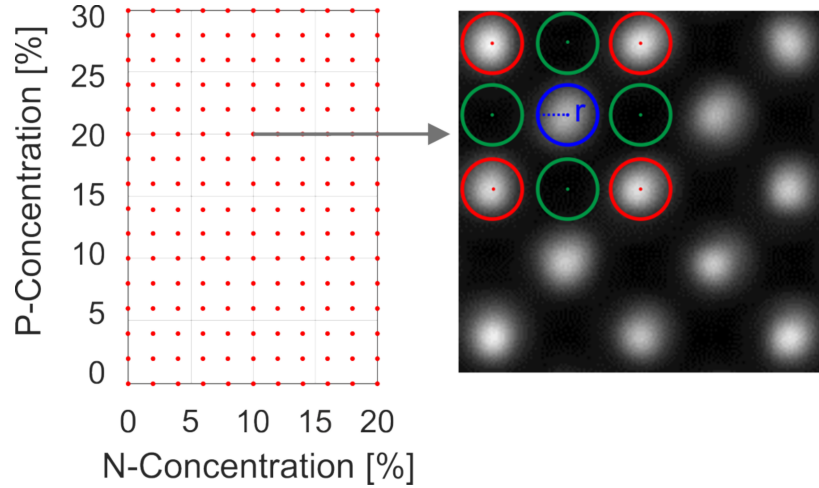


Figure 1: A scheme of the composition set is depicted on the left side. Every red mark represents a full STEM multislice simulation. With given parameters an image can be formed, as displayed on the right side with examples of group III (red), V (blue), and BG column positions (green), and integration radius r .

The intensity of the different atomic columns is obtained by averaging the intensity values in a fixed radius r around the column position. The radius r is chosen in a way that it is big enough to cover the major part

of the atomic column but does not interfere with the surrounding peak integrations. In this work an integration radius of 24 pm was chosen. By averaging the integrated column intensities over approx. 160 columns, three independent mean intensity values $\bar{I}_{III}(N,P)$ for group III, $\bar{I}_V(N,P)$ for group V, and $\bar{I}_{BG}(N,P)$ for the background positions are obtained for each N, P concentration. Applying this procedure to every simulation in the simulation set, with otherwise fixed parameters, three independent maps $I_{III,V,BG}$ are created which we will call *composition maps* from now on. Figure 2 (a) – (c) visualizes all three *composition maps* for a fixed θ_{in-out} with the help of color-coded maps. First we want to focus on the influence of N and P concentration on the STEM intensity. To visualize the effect of the composition on the intensity of the different atomic column positions, it is easier to look at the normalized intensities of the *composition map* rather than the absolute intensities. The normalized intensity of a *composition map*, using the example of a group V column, is calculated via:

$$\frac{\bar{I}_V(N,P)}{\text{mean}(I_V)}.$$

Figure 2 (a) – (c) shows the normalized *composition maps* of group III (a), group V (b), and BG positions (c). Since the sampling of the maps is finite (2 %), the intensity between two composition points is linearly interpolated. All *composition maps* depicted in Figure 2 are built for the HAADF regime. A strong influence of the N composition on the relative intensity deviation is noticeable for the group III column, which is counter-intuitive since it consists of Ga only, while the influence from the P concentration is negligible. This feature is an immediate consequence of the SAD effect and is in very good agreement with the expectation. An N atom on the group V sublattice distorts the crystal locally, resulting in smaller bond lengths to its neighbors. Therefore, the Ga atoms bound to the N atom get distorted from their resting position. Consequently the channeling effect [37] of the beam on a well-aligned atomic column is drastically reduced and the total column intensity of the group III sublattice is spread to a wider region. Keeping the integration radius r constant, the integrated intensity gets smaller accordingly. With

increasing N concentration, this effect becomes stronger and the corresponding group III column intensity decreases. Additionally, the mean atomic number Z on the group V sublattice decreases when the N and the P composition increases, and consequently the group V column intensity decreases. This can be observed in the map of group V depicted in Figure 2 (b). The BG intensity, shown in Figure 2 (c), shows no significant N – P dependency. Distortions induced by N mainly lead to increased diffuse scattering at lower angular regions [38], hence, we also do not expect any influence on the BG for the detector range chosen for Figure 2.

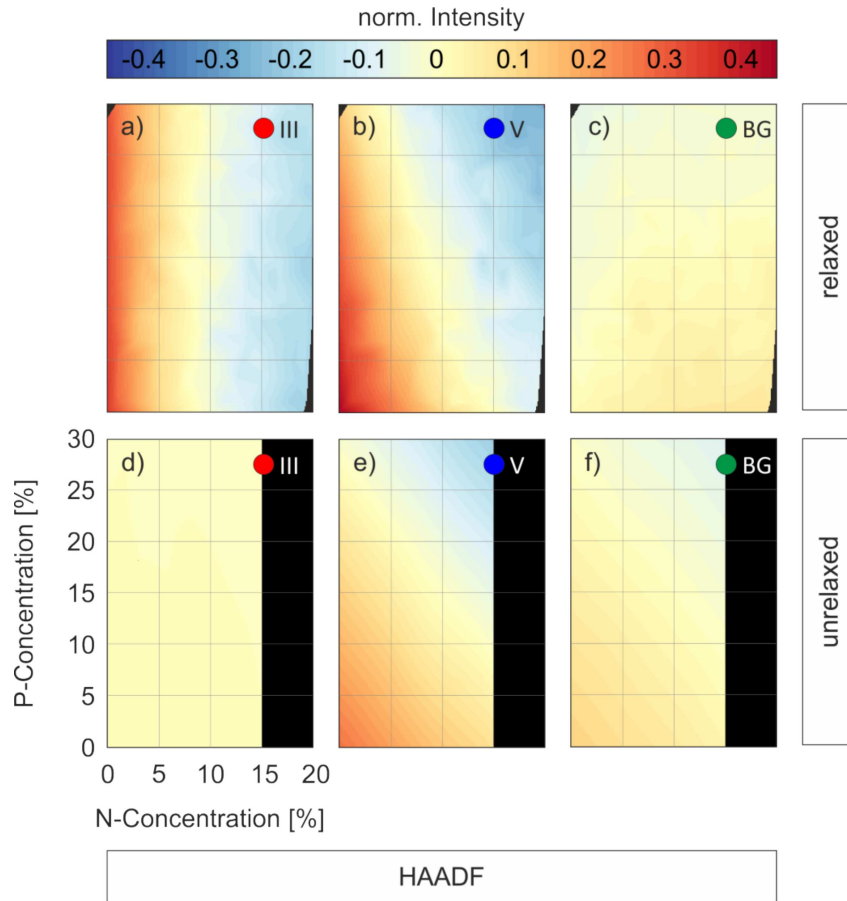


Figure 2: Normalized *composition maps* for the different atom column positions (III, V) as well as the background (BG) for $\theta_{in-out} = 71 - 174$ mrad derived from the relaxed (a) – (c) and unrelaxed (d) – (f) super cells are shown. The values of the color scale represent the relative

deviation of the scattered intensity of a single composition point to the mean value of the map. The composition axes from subfigure (d) correspond to all subfigures in the figure.

From the previous observations, we conclude that the SAD effect projects information about a group V element (N) on the group III lattice intensity. This splits the information from one mixed sublattice to different spatial positions and thus enables us to investigate a material system like Ga(NAsP). In fact, if we would neglect the SAD effect or choose a multinary material system without SAD effect, the information about the individual elements would be mixed on one sublattice. To prove that the SAD effect is responsible for the behavior of the group III, a simulation set with unrelaxed Ga(NAsP) super cells was created. The set was sampled coarser with steps of 5 % in N and 10 % in P – direction. Figure 2 (d) – (f) shows the three *composition maps* built from the unrelaxed super cells. The impact of N on the group III intensity, observed in Figure 2 (a), is not visible anymore in the unrelaxed *composition map* in (d). Since the concentration change solely happens on the group V lattice, this is the only map where we can find the influence of N and P concentration on the intensity. Map (e) is nearly identical to the one observed in Figure 2 (b), representing the decreasing mean atomic number Z of the group V sublattice. Because of TDS, the BG map (f) also follows the decreasing mean atomic number Z. This means that a composition quantification is impossible with the maps built from the unrelaxed super cells. As local distortions evoke an increase of diffuse scattering in lower angular regions, hence, we will investigate the corresponding maps, relaxed and unrelaxed, for the LAADF regime, in the following.

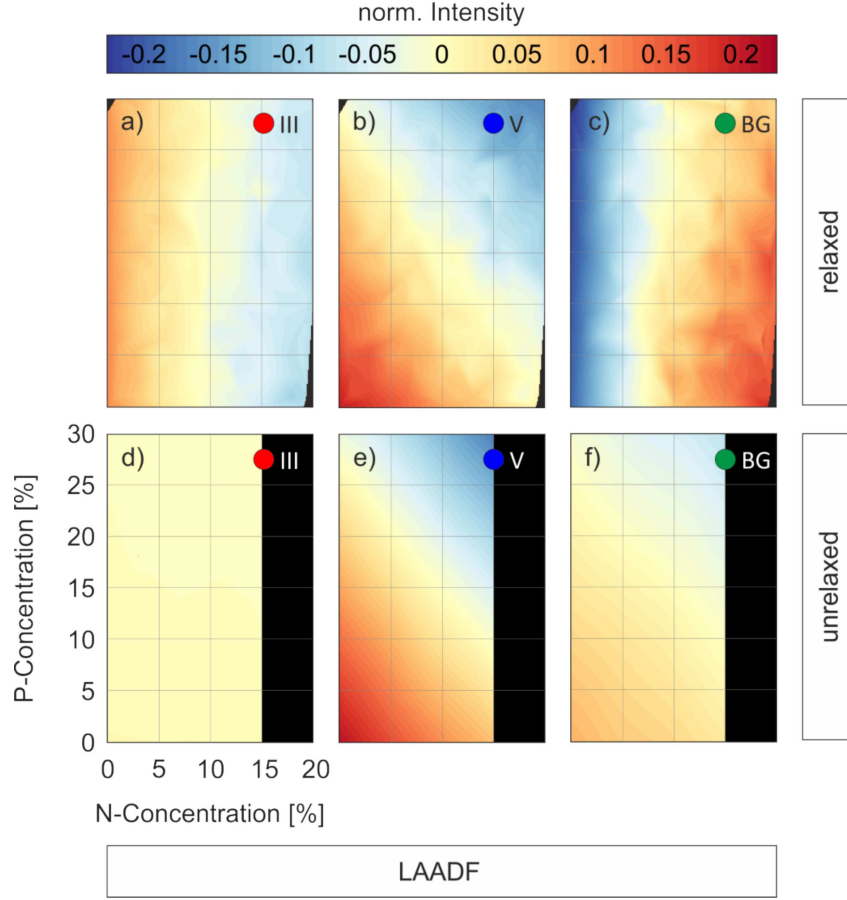


Figure 3: Normalized *composition maps* for the different atomic column positions (III, V) as well as the background (BG) for $\theta_{in-out} = 34 - 136$ mrad derived from the relaxed (a) – (c) and unrelaxed (d) – (f) super cells are shown. The Background shows a much stronger influence on the N – composition compared to Figure 2. The composition axes from subfigure (d) correspond to all subfigures in the figure.

Figure 3 (a) – (c) shows the *composition maps* for the LAADF regime built from the relaxed super cells. The course of the group III map for the low detector inner angle is very similar to the map of the large detector inner angle. Also group V (b) shows the same trend that is observed in Figure 2 (b). However, it should be pointed out that the color scale of the maps changes. The largest deviation from the mean value can be found at the background positions (c). This drastically depends on the N – composition which can be attributed to the SAD effect. The Ga atoms are shifted away from their ideal column position to the off-column positions. The on-column intensity is spread in a wider region, adding more intensity to the

background. With increasing N content the group III intensity decreases and more intensity is scattered into the background, which is especially visible in low angle regions. To underpin this finding, we will present the corresponding *composition maps* derived from the unrelaxed cells in the following, where we do not expect the previous behavior of the group III intensity, since every atom is still on its resting position in the crystal. The *composition maps* built from the unrelaxed simulation set for the LAADF regime are depicted in Figure 3 (d) – (f). No significant changes compared to the *composition maps* built from the unrelaxed simulation set shown in Figure 2 (d) – (f) are noticeable except that the color scale is slightly different. The change of intensity still occurs on the group V lattice only, originating from the change of mean atomic number Z by intermixing from N and P with As. To sum up the observations gained from Figure 2 and Figure 3, we saw that the lattice distortion evoked by N yields information about a group V element on group III positions. Furthermore, information about the N concentration can be extracted from the off-column positions at low detector angles. Also, the intensity scales with the percentage of the element that is responsible for the lattice distortion. This enables us to determine the N and P concentration independently from each other.

In the following paragraph, we want to present an algorithm that combines the gained information from different column position as well as from different θ_{in-out} to determine the composition of the sample.

The main goal of the algorithm is to find the smallest deviation between input values $\bar{I}_{III,V,BG}^{\exp}(\theta_{in-out})$ and the *composition maps* $I_{III,V,BG}(\theta_{in-out})$. Therefore, the first step is to build the *deviation maps* for the individual *composition maps* via:

$$I_{III}^{\Delta}(\theta_{in-out}) = \frac{|I_{III}(\theta_{in-out}) - \bar{I}_{III}^{\exp}(\theta_{in-out})|}{I_{III}(\theta_{in-out})}.$$

Figure 4 shows the *deviation maps* $I_{III,V,BG}^{\Delta}$ for exemplarily chosen input values $\bar{I}_{III,V,BG}^{\exp}(\theta_{in-out})$ obtained from a $\text{Ga}(\text{N}_5\text{As}_{75}\text{P}_{20})$ simulation for the HAADF as well as the LAADF regime with a thickness

chosen to be 20 nm. When using real STEM images the sample thickness has to be determined very carefully to account for thickness difference caused by sample preparation. Many different methods have been proposed to determine the sample thickness, for example by comparing HAADF intensity to adequate multislice simulations [12] or using electron energy loss spectroscopy (EELS) [39]. The color scale in Figure 4 now represents the relative deviation between the input value and the *composition maps*, starting at 0 (in dark blue) for perfect agreement.

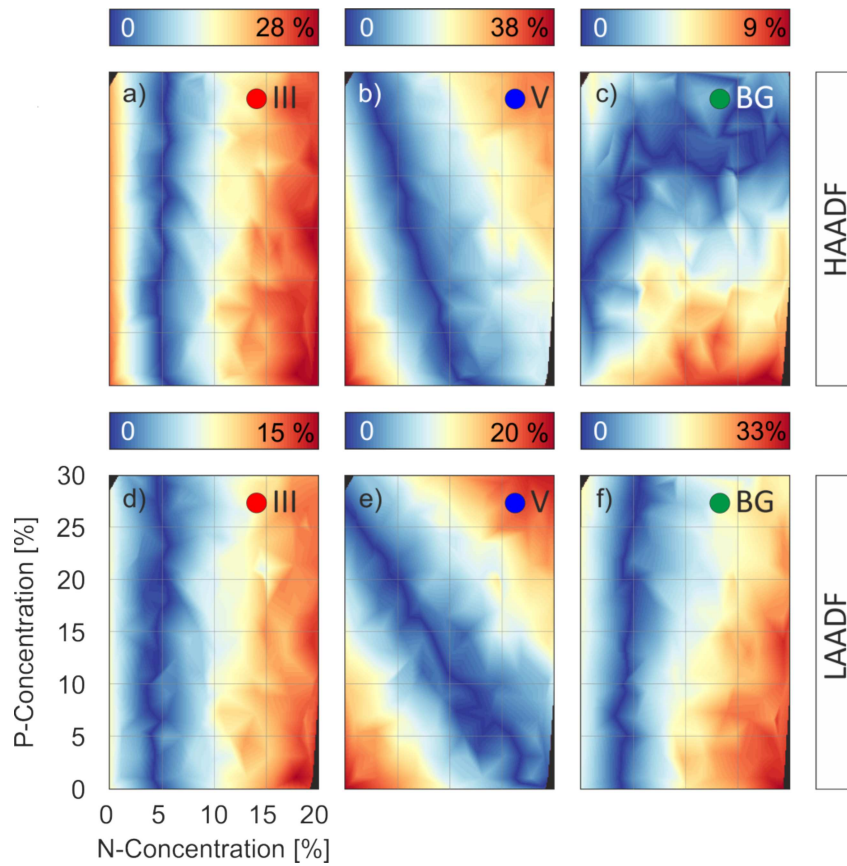


Figure 4: The *deviation maps* for an example $\text{Ga}(\text{N}_5\text{As}_{75}\text{P}_{20})$ composition are displayed for the individual atomic columns in the HAADF (a) – (c) as well as the LAADF (d) – (f) regime. The color scale represents relative deviation between the input values and the corresponding *composition map*. The composition axes from subfigure (d) correspond to all subfigures in the figure.

Map I_{III}^{Δ} (HAADF) (a) shows the smallest deviation for an N concentration of approx. 5 % which is independent of the P concentration. The same behavior can be seen in the I_{III}^{Δ} (LAADF) (d) map. With this information, we certainly know that the input intensities have to come from a material with approx. 5 % N but have no information about the P content up to now. The Maps from I_V^{Δ} (HAADF) (b) and I_V^{Δ} (LAADF) (e) both show the smallest deviation on a diagonal line with slightly different slopes but both crossing the 20 % P point. If we would now combine the maps from I_{III}^{Δ} (HAADF) & I_{III}^{Δ} (LAADF) (a) & (d) and I_V^{Δ} (HAADF) & I_V^{Δ} (LAADF) (b) & (e) without the I_{BG}^{Δ} (c) & (f), the information would be sufficient to determine the input composition to 5 % N and 20 % P. But this is just the case for the example of Ga(NAsP) with N having a tremendous influence on these maps. Additional information will enhance the accuracy of the determination. Thus, we define the *total deviation map* I_{total}^{Δ} as follows:

$$I_{total}^{\Delta} = \frac{\sum_{j=1}^M I_{III}^{\Delta}(\theta_j) + I_V^{\Delta}(\theta_j) + I_{BG}^{\Delta}(\theta_j)}{3 \cdot M},$$

where the used detector ranges are represented by $\theta_1 \dots \theta_M$. There is the option of weighting the individual *deviation maps* $I_{III,V,BG}^{\Delta}$ with respect to each other, which will be tackled in further studies. This *total deviation map* now represents the combined relative deviations between the input values $\bar{I}_{III,V,BG}^{\exp}(\theta_{in-out})$ and the *deviation maps* $I_{III,V,BG}^{\Delta}(\theta_{in-out})$ for different detector ranges. In this *total deviation map* we can now identify the global minimum of all individual maps at once, which gives us the N and P concentration with the best agreement between input values and individual *deviation maps*. To check if the algorithm is self-consistent, a sanity check was performed, with the results of I_{total}^{Δ} depicted in Figure 5. For this check, simulated images for fixed N-P compositions, namely Ga(N₅As₇₅P₂₀) (a) & (d), Ga(N₁₅As₆₅P₂₀) (b) & (e) and Ga(N₁₀As₈₀P₁₀) (c) & (f), were created and treated like experimentally acquired

images. The maps $I_{\text{total}}^{\Delta}$ are depicted as contour plots with a spacing of 1%, which means that every N-P point included in a colored plateau surrounded by a black line has the same total deviation from the input values within a tolerance of 1%. This leads to distinct areas, which represent N-P compositions that differ around a chosen uncertainty. The red crosses represent the total minima of the map obtained using the procedure described above. Figure 5 (a) – (c) shows $I_{\text{total}}^{\Delta}$, created with the relaxed *composition maps*. The total minima of the maps (a) – (c) show perfect agreement with the chosen input compositions, which demonstrates that the algorithm is self-consistent. The area around the global minimum is elongated elliptically, with a larger radius in the P-axis with approx. 4% uncertainty and a smaller radius along the N-axis with approx. 2% uncertainty. This indicates that the P content is harder to determine accurately compared to the N content, due to the bigger difference in atomic number and the SAD induced by N.

The sanity check was also performed with the *composition maps* built from the unrelaxed super cells with the resulting *total deviation maps* $I_{\text{total}}^{\Delta}$ depicted in Figure 5 (d) – (e). A very broad diagonal stripe that represents 1 % uncertainty around the input composition is visible in every map. This means that every composition within that stripe is equally possible for this set of input values. Since the group III and BG intensities (Figure 2 (d) & (f)) from the *composition maps* created from the unrelaxed super cells show no significant dependency on the N or P content, the *total deviation maps* $I_{\text{total}}^{\Delta}$ are dominated by the course of the group V maps (Figure 2 (e)). With this intensity information it is not possible to determine the composition of a material with different elements mixed on one sublattice accurately. Furthermore, the overall gradient of the maps built from the unrelaxed super cell set, shown in Figure 5 (d) – (f), is less steep than the maps created with the relaxed super cell set depicted in Figure 5 (a) – (c).

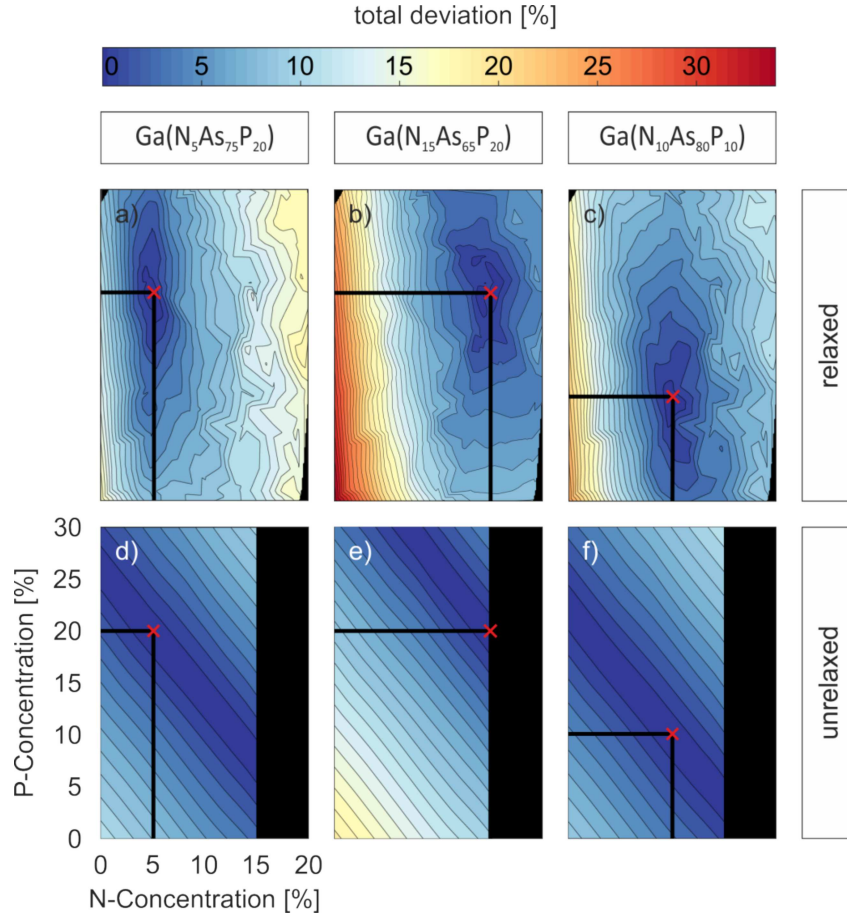


Figure 5: Sanity Check of the algorithm with three different input compositions. The *total deviation maps* show a minimum area of total deviation around the input composition. The red cross marks the global minimum of the map and thus the calculated N-P composition. The black lines represent plateaus with 1 % error steps. The composition axes from subfigure (d) correspond to all subfigures in the figure.

In summary, the sanity check performed with the *composition maps* built from the relaxed super cells shows that it is possible to determine the concentration of a quaternary semiconductor alloy with STEM image intensities, even when the intermixing of the atoms solely happens on one sublattice. This is possible because the SAD effect evoked by N projects information about a group V element (N) onto the group III sublattice.

Of course, the algorithm will be applied to experimental images in the future with the goal to gain highly resolved information on the composition for quaternary semiconductor alloys.

Summary

In this work, we presented a method to determine the composition of a quaternary III/V semiconductor alloy by comparing its HAADF STEM images to a set of STEM image simulations with systematically varied elemental composition. The simulation cells were prepared carefully, including VFF relaxation to account for SAD effects. Due to the high number of simulations needed for a profound simulation set, the simulations had to run on a high performance computing cluster. For the model system Ga(NAsP), the N atoms change the group III column intensity provoked by the SAD effect, since this behavior is not visible using unrelaxed simulation cells. With the information from the group III sublattice and the group V sublattice, it is already possible to determine the composition. Additional measurements, especially at lower detector angular ranges, improve the accuracy of the method presented here. Therefore, we combined *deviation maps* $I_{III,V,BG}^{\Delta}$ from multiple θ_{in-out} to take care of all dependencies at once. In the end, we presented a successful sanity check with three exemplarily chosen Ga(NAsP) alloys to check whether our algorithm is self-consistent. With this we could show that it is possible to determine the concentration of a quaternary semiconductor alloy via STEM images at atomic resolution without further information from any supplementary method. This method has great potential to be implemented in the standard workflow when investigating semiconductor alloys with STEM.

Acknowledgement

Support by the German Research Foundation (DFG) in the framework of the research training group “Functionalization of Semiconductors” (GRK 1782) is gratefully acknowledged.

References

- [1] L. De Caro, C. Giannini, L. Tapfer, Determination of the lattice strain and chemical composition of semiconductor heterostructures by high-resolution x-ray diffraction, *J. Appl. Phys.* 79 (1996) 4101. doi:10.1063/1.361773.
- [2] W. Li, M. Pessa, J. Likonon, Lattice parameter in GaNAs epilayers on GaAs: Deviation from Vegard's law, *Appl. Phys. Lett.* 78 (2001) 2864–2866. doi:10.1063/1.1370549.
- [3] S. Raj, Vegard ' s law : a fundamental relation, 98 (2007) 776–779.
- [4] J.M. Tilli, H. Jussila, K.M. Yu, T. Huhtio, M. Sopanen, Composition determination of quaternary GaAsPN layers from single X-ray diffraction measurement of quasi-forbidden (002) reflection, *J. Appl. Phys.* 115 (2014). doi:10.1063/1.4878939.
- [5] D.O. Klenov, S.D. Findlay, L.J. Allen, S. Stemmer, Influence of orientation on the contrast of high-angle annular dark-field images of silicon, (n.d.). doi:10.1103/PhysRevB.76.014111.
- [6] J.M. Lebeau, S.D. Findlay, L.J. Allen, S. Stemmer, Quantitative atomic resolution scanning transmission electron microscopy, *Phys. Rev. Lett.* 100 (2008) 1–4. doi:10.1103/PhysRevLett.100.206101.
- [7] J.M. LeBeau, S. Stemmer, Experimental quantification of annular dark-field images in scanning transmission electron microscopy, *Ultramicroscopy*. 108 (2008) 1653–1658. doi:10.1016/j.ultramic.2008.07.001.
- [8] A. Rosenauer, K. Gries, K. Müller, A. Pretorius, M. Schowalter, A. Avramescu, K. Engl, S. Lutgen, Measurement of specimen thickness and composition in $\text{Al}_x\text{Ga}_{1-x}\text{N}$ / GaN using high-angle annular dark field images, *Ultramicroscopy*. 109 (2009) 1171–1182. doi:10.1016/j.ultramic.2009.05.003.

- [9] J.M. Cowley, a. F. Moodie, The scattering of electrons by atoms and crystals. I. A new theoretical approach, *Acta Crystallogr.* 10 (1957) 609–619. doi:10.1107/S0365110X57002194.
- [10] T. Grieb, K. Müller, R. Fritz, M. Schowalter, N. Neugebohrn, N. Knaub, K. Volz, A. Rosenauer, Determination of the chemical composition of GaNAs using STEM HAADF imaging and STEM strain state analysis, *Ultramicroscopy*. 117 (2012) 15–23. doi:10.1016/j.ultramic.2012.03.014.
- [11] T. Grieb, K. Müller, R. Fritz, V. Grillo, M. Schowalter, K. Volz, A. Rosenauer, Quantitative chemical evaluation of dilute GaNAs using ADF STEM: Avoiding surface strain induced artifacts, *Ultramicroscopy*. 129 (2013) 1–9. doi:10.1016/j.ultramic.2013.02.006.
- [12] A. Rosenauer, K. Gries, K. Müller, A. Pretorius, M. Schowalter, A. Avramescu, K. Engl, S. Lutgen, Measurement of specimen thickness and composition in $\text{Al}_x\text{Ga}_{1-x}\text{N}$ / GaN using high-angle annular dark field images, *Ultramicroscopy*. 109 (2009) 1171–1182. doi:10.1016/j.ultramic.2009.05.003.
- [13] T. Wegele, A. Beyer, P. Ludewig, P. Rosenow, L. Duschek, K. Jandieri, R. Tonner, W. Stolz, K. Volz, Interface morphology and composition of Ga(NAsP) quantum well structures for monolithically integrated LASERs on silicon substrates, *J. Phys. D. Appl. Phys.* 49 (2016) 75108. doi:10.1088/0022-3727/49/7/075108.
- [14] N. Knaub, A. Beyer, T. Wegele, P. Ludewig, K. Volz, Quantification of Bi distribution in MOVPE-grown Ga(AsBi) via HAADF STEM, *J. Cryst. Growth*. 433 (2016) 89–96. doi:10.1016/j.jcrysgro.2015.10.007.
- [15] S.J. Pennycook, Z-contrast stem for materials science, *Ultramicroscopy*. 30 (1989) 58–69. doi:10.1016/0304-3991(89)90173-3.
- [16] A. Rosenauer, M. Schowalter, STEMSIM - A New Software Tool for Simulation of STEM HAADF Z-

- Contrast Imaging, *Microsc. Semicond. Mater.* 2007. Springer P (2008) 170–172. doi:10.1007/978-1-4020-8615-1_36.
- [17] S.J. Pennycook, D.E. Jesson, High-resolution Z-contrast imaging of crystals, *Ultramicroscopy*. 37 (1991) 14–38. doi:10.1016/0304-3991(91)90004-P.
- [18] A. Rosenauer, T. Mehrtens, K. Müller, K. Gries, M. Schowalter, P. Venkata Satyam, S. Bley, C. Tessarek, D. Hommel, K. Sebald, M. Seyfried, J. Gutowski, A. Avramescu, K. Engl, S. Lutgen, Composition mapping in InGa_N by scanning transmission electron microscopy, *Ultramicroscopy*. 111 (2011) 1316–1327. doi:10.1016/j.ultramic.2011.04.009.
- [19] K. Müller-Caspary, O. Oppermann, T. Grieb, F.F. Krause, A. Rosenauer, M. Schowalter, T. Mehrtens, A. Beyer, K. Volz, P. Potapov, Materials characterisation by angle-resolved scanning transmission electron microscopy, *Sci. Rep.* 6 (2016) 37146. doi:10.1038/srep37146.
- [20] D.B. Jackrel, S.R. Bank, H.B. Yuen, M.A. Wistey, J.S. Harris, A.J. Ptak, S.W. Johnston, D.J. Friedman, S.R. Kurtz, Dilute nitride GaInNAs and GaInNAsSb solar cells by molecular beam epitaxy, *J. Appl. Phys.* 101 (2007). doi:10.1063/1.2744490.
- [21] T. Grieb, K. Müller, E. Cadel, A. Beyer, M. Schowalter, E. Talbot, K. Volz, A. Rosenauer, Simultaneous Quantification of Indium and Nitrogen Concentration in InGa_NAs Using HAADF-STEM, *Microsc. Microanal.* 20 (2014) 1740–1752. doi:10.1017/S1431927614013051.
- [22] V. Grillo, K. Mueller, K. Volz, F. Glas, T. Grieb, A. Rosenauer, Strain, composition and disorder in ADF imaging of semiconductors, *J. Phys. Conf. Ser.* 326 (2011) 12006. doi:10.1088/1742-6596/326/1/012006.
- [23] S. Liebich, M. Zimprich, A. Beyer, C. Lange, D.J. Franzbach, S. Chatterjee, N. Hossain, S.J. Sweeney, K. Volz, B. Kunert, W. Stolz, Laser operation of Ga(NAsP) lattice-matched to (001) silicon

- substrate, Appl. Phys. Lett. 99 (2011) 1–4. doi:10.1063/1.3624927.
- [24] B. Kunert, K. Volz, J. Koch, W. Stolz, Direct-band-gap Ga (NAsP)-material system pseudomorphically grown on GaP substrate, Appl. Phys. Lett. 88 (2006) 182108.
 - [25] S. Wirths, R. Geiger, N. Von Den Driesch, G. Mussler, T. Stoica, S. Mantl, Z. Ikonc, M. Luysberg, S. Chiussi, J.M. Hartmann, Lasing in direct-bandgap GeSn alloy grown on Si, Nat. Photonics. 9 (2015) 88–92.
 - [26] P.N. Keating, Effect of invariance requirements on the elastic strain energy of crystals with application to the diamond structure, Phys. Rev. 145 (1966) 637–645.
doi:10.1103/PhysRev.145.637.
 - [27] V. Grillo, E. Carlino, F. Glas, Influence of the static atomic displacement on atomic resolution Z-contrast imaging, Phys. Rev. B - Condens. Matter Mater. Phys. 77 (2008) 1–6.
doi:10.1103/PhysRevB.77.054103.
 - [28] J.O. Oelerich, L. Duschek, J. Belz, A. Beyer, S.D. Baranovskii, K. Volz, STEMsalabim: A high-performance computing cluster friendly code for scanning transmission electron microscopy image simulations of thin specimen, Submitt. Publ. (2016). <http://www.online.uni-marburg.de/stemsalabim/>.
 - [29] E.J. Kirkland, Advanced computing in electron microscopy, J. Appl. Cryst. 32 (1999) 378–379.
 - [30] E.J. Kirkland, Image Simulation in Transmission Electron Microscopy, Simulation. (2006) 1–14.
 - [31] B.D. Forbes, A.J. D’Alfonso, S.D. Findlay, D. Van Dyck, J.M. LeBeau, S. Stemmer, L.J. Allen, Thermal diffuse scattering in transmission electron microscopy, Ultramicroscopy. 111 (2011) 1670–1680.
doi:10.1016/j.ultramic.2011.09.017.
 - [32] A. Beyer, J. Belz, N. Knaub, K. Jandieri, K. Volz, Influence of spatial and temporal coherences on

- atomic resolution high angle annular dark field imaging, *Ultramicroscopy*. 169 (2016) 1–10.
doi:10.1016/j.ultramic.2016.06.006.
- [33] C. Dwyer, R. Erni, J. Etheridge, Method to measure spatial coherence of subangstrom electron beams, *Appl. Phys. Lett.* 93 (2008). doi:10.1063/1.2957648.
- [34] C. Dwyer, R. Erni, J. Etheridge, Measurement of effective source distribution and its importance for quantitative interpretation of STEM images, *Ultramicroscopy*. 110 (2010) 952–957.
doi:10.1016/j.ultramic.2010.01.007.
- [35] D.T. Nguyen, S.D. Findlay, J. Etheridge, The spatial coherence function in scanning transmission electron microscopy and spectroscopy, *Ultramicroscopy*. 146 (2014) 6–16.
doi:10.1016/j.ultramic.2014.04.008.
- [36] Unidata, Network Common Data Form (NetCDF), (2016). doi:10.5065/D6H70CW6.
- [37] V. Grillo, The effect of surface strain relaxation on HAADF imaging, *Ultramicroscopy*. 109 (2009) 1453–1464. doi:10.1016/j.ultramic.2009.07.010.
- [38] V. Grillo, K. Mueller, K. Volz, F. Glas, T. Grieb, A. Rosenauer, Strain, composition and disorder in ADF imaging of semiconductors, *J. Phys. Conf. Ser.* 326 (2011) 12006. doi:10.1088/1742-6596/326/1/012006.
- [39] R.F. Egerton, M. Malac, EELS in the TEM, *J. Electron Spectros. Relat. Phenomena*. 143 (2005) 43–50. doi:10.1016/j.elspec.2003.12.009.